Post-deformational annealing at the subgrain scale: Temperature dependent behaviour revealed by in-situ heating experiments on deformed single crystal halite

V.E. Borthwick*, S. Piazolo

Department of Geology and Geochemistry, Stockholm University, Svante Arrhenius väg 8C, Stockholm 10691, Sweden

ABSTRACT

The dynamics of substructures, which encompass all structures present at the subgrain-scale, were investigated by static, in-situ annealing experiments. Deformed, single crystal halite was annealed inside a scanning electron microscope at temperatures between 280 and 470 °C. Electron backscatter diffraction maps provided detailed information about crystallographic orientation changes. Three temperature dependent regimes were distinguished based on boundary misorientation changes. In regime I (280–300 °C) some low angle boundaries (LABs), i.e. with 1°–15° misorientation, increase in misorientation angle, while others decrease. In regime II (~300 °C) all LABs undergo a decrease in misorientation angle. Regime III (>300 °C) is defined by enhancement of the subgrain structure as remaining LABs increase and some undergo a rotation axis change. Throughout regimes I and II, new LABs develop, subdividing subgrains. LABs could be divided into four categories based on annealing behaviour, orientation and morphology. We suggest that these observations can be directly related to the mobility and activation temperature of climb of two dislocation groups introduced during deformation. Therefore, with in-depth investigation of a substructure with known deformation geometry, we can infer ratios of dislocation types and their post-deformation and post-annealing location. These can potentially be used to estimate the post-deformational annealing temperature in crystalline materials.

© 2010 Elsevier Ltd. All rights reserved.

1. Introduction

Interpretation of microscale behaviour is key to developing a greater understanding of tectonic processes. Examination of the microstructure of a rock can give insight into the processes that occurred during its deformation history and the conditions under which these processes took place. The inherent problem in microstructural interpretation is that we are viewing the "frozen-in" final microstructure, a result of the accumulation of a sequence of processes. In particular, post-deformational annealing can drastically change the microstructure by growth of new strain-free grains and reorganisation of grain boundaries (e.g. Heilbronner and Tullis, 2002). However, at the same time, these changes have the potential to provide evidence of the time-temperature path of the rock, as well as its rheological evolution.

An important part of post-deformational annealing is substructural rearrangement. Deformation is accommodated by the storage of defects in the crystal lattice. Strain energy is stored as point defects, dislocations and dislocation arrays (subgrain boundaries or grain boundaries) (Passchier and Trouw, 2005). The driving force for post-deformational annealing is the reduction of the stored energy of the system (Urai et al., 1986; Drury and Urai, 1990; Baker, 2000). This recovery is driven by the interaction of dislocations via their long-range stress fields and occurs through two main processes, annihilation of dislocations of opposite signs and polygonisation, where dislocations align to form low energy arrays (LABs) (Gottstein, 2004; Humphreys and Hatherly, 2004). As dislocations align, their areas of distortion overlap so that, with increasing misorientation the energy per dislocation decreases (Hull and Bacon, 2001). These processes are facilitated by dislocation climb, which is thermally activated and can limit mobility at lower temperatures. In particular, climb is important for dislocations in a boundary to rearrange to decrease spacing (Hull and Bacon, 2001). Once a polygonised substructure is attained, the stored energy can be further lowered by a coarsening of the substructure to reduce total boundary area (Humphreys and Hatherly, 2004). In particular, symmetrical tilt boundaries can move by glide of the edge dislocations that comprise the boundary (Humphreys and Hatherly, 2004). Mobility in this case is high, and

---

* Corresponding author. Fax: +46 (0) 8 6747897.
E-mail address: verity.borthwick@geo.su.se (V.E. Borthwick).

boundary migration can occur even at low temperatures (Parker and Washburn, 1952). It is important to note that the energies of LABs are strongly dependent on both misorientation and the boundary plane; therefore changes in the misorientation and/or boundary plane may also result in energy reduction even if the total grain boundary length increases (Piazolo et al., 2004).

LABs have in general not received as much attention as high angle grain boundaries in geological materials. Previous experiments carried out on polycrystalline halite (Bestmann et al., 2005; Piazolo et al., 2006) indicated that substructural elements did not behave exactly as predicted by the above outlined classical theory, where LABs are generally expected to undergo a stable increase in misorientation once formed, progressing on to subgrain growth to reduce the total boundary length (Humphreys and Hatherly, 2004). Bestmann et al. (2005) and Piazolo et al. (2006) observed LABs both increasing and decreasing in misorientation, rearranging within grains as well as in some cases dissipating completely.

Recently developed techniques in the field of microstructural analysis enable us to investigate substructural behaviour in more detail. Electron backscatter diffraction (EBSD) (Prior et al., 1999 and references therein) allows us to fully characterise misorientation axes and angles between grains and subgrains. There have been a number of studies of microstructures taken from various stages of annealing in both geological materials (e.g. calcite) (Barnhoorn et al., 2005) and metals (Ferry and Humphreys, 1996, 2006; Huang and Humphreys, 2000, 2001; Huang et al., 2000). In-situ heating within the scanning electron microscope (SEM) (Le Gall et al., 1999) and analysis with EBSD are thus an essential addition, providing a powerful tool for "real-time" microanalysis of structural changes during annealing (Humphreys, 2001; Seward et al., 2002; Piazolo et al., 2005). At present a handful of studies have been carried out using this method, on materials including titanium (Seward et al., 2004), aluminium (Huang and Humphreys, 1999; Piazolo et al., 2005; Kirch et al., 2008) rocksalt (Bestmann et al., 2005; Piazolo et al., 2006), copper (Mirpuri et al., 2006; Field et al., 2007) and Al–Mn alloys (Lens et al., 2005).

NaCl was chosen as the experimental material for this study. Halite plays a significant role in fold-and-thrust belts, delta tectonics, basin evolution and hydrocarbon accumulation, as well as being a possible medium for storage of nuclear waste (Franssen, 1993 and references therein; Rempe, 2007; Schléder and Urai, 2007). The development of subgrain-scale microstructures in halite occurs at experimentally attainable conditions ($\sim$20 MPa and >200 °C) (Senseny et al., 1992) and is similar to that occurring at higher temperatures and pressures in silicates, making it a good analogue material (Guillope and Poirier, 1979; Drury and Urai, 1990). Due to its ionic-bonded, cubic crystal structure, NaCl provides a simple starting point for studying these complex processes.

In this contribution, we aim to provide a comprehensive characterisation of the substructural dynamics of a crystalline geological material during post-deformational annealing. On the basis of this information we attempt to recognise key features occurring at different annealing temperatures, which may be used for interpreting post-deformational annealing conditions in natural samples. In particular, by recognising different types of LABs and their respective behaviour during annealing we aim to improve our understanding of substructural development.

2. Methods

2.1. Sample preparation

The sample (TL1) was prepared from a single crystalline rod of melt grown high purity sodium chloride provided by *Harshaw Chemical Co.* (van der Linden, 2002). Using a single crystal removed

the possibility of rapid high angle grain boundary migration removing the substructure (Piazolo et al., 2006) and the high purity meant that boundary pinning by impurities would be less likely to occur (Smith, 1948). Rectangular samples with a size of $\sim$7 × 10 × 15 mm were cleaved along {100} faces. These particular edge ratios were chosen to limit dislocation glide to two sets of perpendicular planes (Fig. 1a) (Davidge and Pratt, 1964). Due to the asymmetry of the sample one set of glide planes will be activated more easily. With this chosen geometry the sample is more relevant to geological materials with low symmetry crystallography, which tend to have a well-developed dominant slip system with a number of subsidiary slip systems.

The single crystals were deformed as follows: during a period of four days the sample was heated in steps of 20–25 °C per hour to a maximum temperature of 660 °C. After heating, the sample was cooled to the deformation temperature of 453 °C. TL1 was then deformed under uniaxial compression to a final strain of 0.165 at a strain rate of 6.9 × $10^{-6}s^{-1}$. After deformation the sample was unloaded and allowed to cool to room temperature, taking $\sim$1 h. As fluid content at the boundaries can have a large effect on boundary mobility, the samples were kept dry in a desiccator to reduce the possibility of atmospheric absorption of water. Sections of deformed halite (6 × 5.5 × 1.5 mm) were cleaved using a razor-blade (Fig. 1b). The cleaved surfaces gave good quality electron backscatter diffraction patterns (EBSPs).

2.2. Experimental setup

The analysis areas for in-situ annealing experiments were selected close to the centre of each slice, where deformation was most intense (Fig. 1b). Two main areas of interest were chosen, areas in the central deformation zone (CDZ), where subgrains were near equiaxed and numerous (Fig. 1c) and areas in more peripheral zones (PZ) where subgrains were organised into elongate bands (Fig. 1d). The annealing experiments were performed in an XL30 environmental field emission gun SEM. Samples were held in place on the heating stage by a metal plate which served to increase the connectivity of the sample to the heating stage (Fig. 2a). Sample TL1_A2 had some dry silver paint on the bottom surface, which may have slightly increased conduction to the sample. In correspondence with annealing behaviour we estimate that this resulted in an increase of $\sim$10 °C at the sample surface and furnace temperatures have been adjusted for this. The sample was tilted at a 70° angle to the electron beam to optimise the EBSD signal. The sample temperatures are estimated to be within ±15 °C of the furnace temperature. Furnace temperatures are quoted in this paper; samples were heated under high vacuum ($\sim$5.4 × 10^{-6} mBar) to temperatures of 280–470 °C in a number of steps. A number of different heating approaches were taken (Fig. 2b). We chose to investigate annealing at temperatures below that of the experimental deformation temperature (i.e. 453 °C) in order to examine a deformation-temperature-time path that is experienced commonly by natural rocks. Rocks are generally deformed in a ductile manner at depth at high temperatures. When deformation ceases the rock is subject to lower than deformation temperatures for long periods. In order to separate distinctive behaviour at differing temperatures it was necessary to steadily increase the temperature of annealing towards that of deformation. Had we started at higher temperatures, evidence of lower temperature regimes, which may be significant in natural settings would have been erased.

2.3. Data acquisition

EBSD mapping was conducted during annealing to gather information about changes in crystallographic orientation. Analysis areas with a high density of subgrains were selected from examination
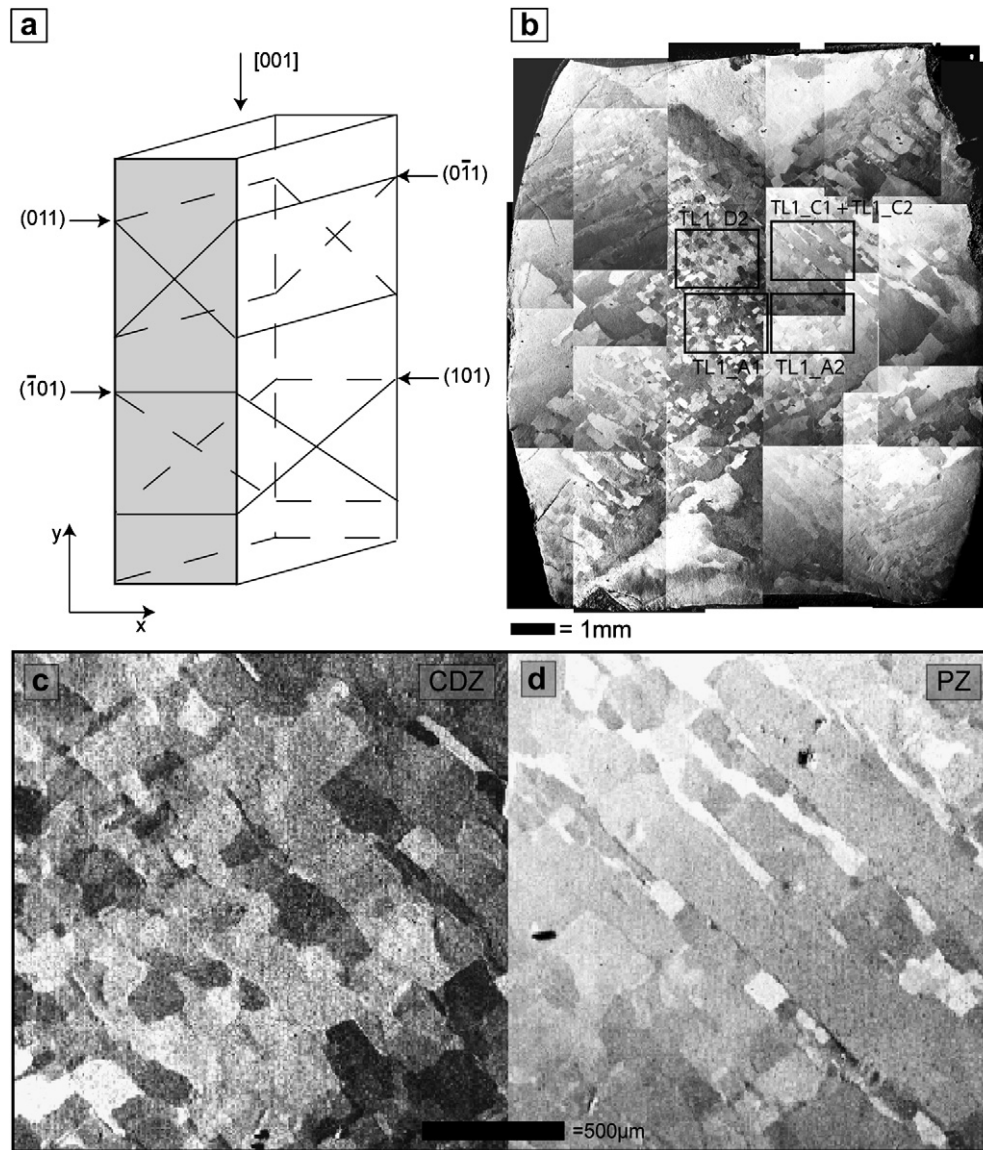
Fig. 1. (a) Slip systems in NaCl. In single crystals, deformation usually initiates on one set of planes, which subsequently dominate the deformation: if slip occurs on both planes e.g. (011) and (0$\bar{1}$1) then the crystal develops a barrelled shape in the (010) section (shaded) (after Davidge and Pratt, 1964). (b) composite forescatter images of a complete polished section of the TL1 sample; approximate analyses areas are highlighted. TL1_A1 and A2, and TL1_D2 are located in the centrally deformed zone while TL1_C1 and C2 are from the peripheral zone. (c) and (d) show detailed orientation contrast images of (c) the centrally deformed zone with near equiaxed subgrains and (d) the peripheral zone with elongate bands. Compression axis is vertical for all images.

of orientation contrast images (Fig. 1b) (Prior et al., 1996). Large maps (~1.9 × 1.5 mm) were taken before heating and after each heating stage when the samples had been cooled to ~30 °C over a period of ~2 h. During heating, small area maps (~0.17 × 0.17 mm) were also taken every 10 min to observe changes occurring. If significant changes were detected, the heating process was immediately halted. At temperatures higher than ~400 °C, during heating mapping became impossible, as the EBSP signal degraded. Charging generally did not occur at room temperature but where present, heating to ~100 °C solved the problem. EBSD patterns were obtained using a 12 kV accelerating voltage and a beam current of 2 nA, at a working distance of 15 mm. Samples were mapped by beam movement at a step size of 1 μm ensuring there were at least ten data points between adjacent subgrain boundaries. Beam mapping was calibrated on a perfect single crystal of silicon so that the maximum deviation across 1 mm of the sample was <0.5°.

Oxford Instruments HKL technology Channel 5 software was used to collect and analyse EBSD data. Automatic Hough transform analysis picked out the centres of 5–6 Kikuchi bands. Pattern indexing was achieved by comparison of calculated solid angles to a halite match unit containing ~40 to 50 reflectors. The percentage of non-indexed points ranged between 5 and 15%. Cleavage steps were poorly indexed producing artefact boundaries in EBSD maps, with anomalously high misorientations. These were not taken into consideration in subsequent analyses.

2.4. Data analysis and processing

Noise reduction was applied to the data following a procedure whereby non-indexed pixels with up to 6 indexed neighbour pixels were automatically assigned the most common orientation from neighbouring indexed pixels. On average, 8% of pixels in a map were adjusted based on this method. A filter was applied to remove
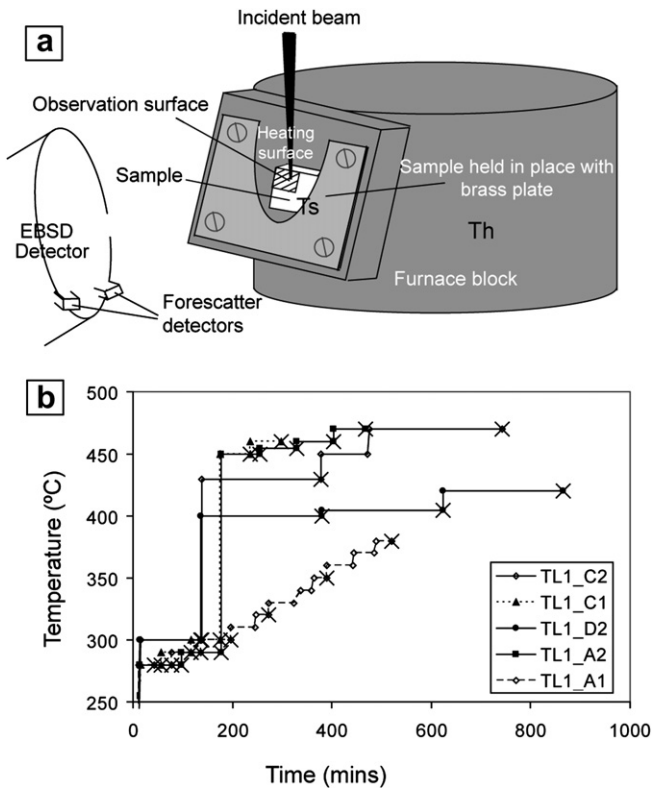
Fig. 2. Experimental setup and methods (a) Sketch of the experimental setup showing an ~2 mm thick slice of NaCl sample, held in place on the heating stage by a screwed on brass plate. The observation surface is equivalent to each of the rectangular selected areas in Fig. 1b. (b) Graph showing different heating procedures used in the experiments. The crosses mark when the sample was cooled to ~30 °C for mapping.

single, isolated pixels having a very different orientation to their surrounding areas. In order to enhance detection of LABs, two passes of a 3 × 3 Kuwahara filter (an edge detection image analysis tool) were used (Kuwahara and Eiho, 1976; Humphreys et al., 2001). To be sure that no artefacts were introduced due to the described noise reduction, data was carefully compared for its reproduction of the grey level changes observed in orientation contrast images of the same area. Fig. 3 shows a comparison of the orientation contrast image (Fig. 3a) to the data after noise reduction has been applied (Fig. 3b) and after noise reduction and Kuwahara filter have been applied (Fig. 3c). The parameters which gave the most accurate representation of the orientation contrast images substructure (Fig. 3) were subgrain detection defined by an angle of 5° and an upper limit smoothing angle of 1.5° (i.e. no filtering was applied to misorientations larger than this angle).

For the purpose of this study we define a LAB as having a misorientation of 1°–15°. Subgrains were defined as areas with a critical boundary of 1° and a forced boundary completion (choosing the highest angle path) if there were small segments below the critical boundary value of 1°. LAB misorientations were determined by taking the pixel-to-pixel misorientation average for an area selected which encompassed one pixel on either side of the LAB, also using a cutoff of 1° (see Fig. A1 for selection method). These were calculated for each heating stage on a number of specific LABs which were followed through the experiment in order to better estimate the rate of misorientation change. The rate of change in misorientation of LABs was calculated by a) obtaining the average misorientation across the boundary for each heating step, b) calculating the rate by dividing the change from one to the next heating step by the length of heating and c) taking the average rate

of change from a number of LABs of that type. Misorientation distributions for the whole analysed areas at different heating stages were compared to determine overall changes in the misorientations of the LABs present. Similar misorientation distributions were taken over an undeformed crystal heated to 300 °C and 450 °C and these showed no significant changes.

Although a background error of 0.3° has been estimated in other studies (Pennock et al., 2002), we suggest a lower value for our experiments. Since the same area was mapped after each stage, the background error was determined to be ±0.1° (see Appendix for error calculations). All misorientation rate changes quoted in this article are subject to this error.

The strength of a fabric (J-index) can be used to evaluate the intensity of the texture (i.e. higher values show clustering of the orientation) (Bunge, 1981; Mainprice and Silver, 1993). J-index values were calculated using orientation distribution functions with the following equation:

$$J = \int f(g)^2 dg \qquad (1)$$

where J is the J-index and $dg = 1/8\pi^2 \sin\varphi d\phi_1 d\phi d\phi_2$. Misorientation axis analysis was applied to the LABs to examine dominant boundary misorientation axes using a minimum misorientation angle of 1°. Greyscale maps representing the deviation of orientation with respect to a reference point were used to compare microstructures between heating stages. The validity of the results with respect to mapping techniques and heating setup is discussed in the Appendix.

3. Results

3.1. Pre-annealing microstructure

The post-deformation, pre-heating substructure of sample TL1 contained well-defined subgrains (Fig. 3d) with the misorientation of enclosing LABs <7°. Areas analysed from the CDZ, the most highly deformed area, showed equiaxed, diamond-shaped subgrains with LABs that form perpendicular to one another and at ~45° angles to the compression axis (Fig. 1c). One set of the perpendicular LABs was better developed, with higher misorientations and greater continuous lengths. A third less frequent set of LABs occurred, primarily in the CDZ often sub-perpendicular to the compression axis. Subgrains surrounded by these LABs tended to have a higher aspect ratio and often exhibited a lensoid shape. Other short segments of LABs (3–13 μm length), generally curved with a low misorientation, occurred throughout the whole sample. In the PZ the number of equiaxed subgrains decreased, with subgrains more commonly arranged into elongate bands with perpendicular LABs of a lower misorientation forming bridges between these bands (Fig. 1d).

3.2. Categories of LABs

LABs could be categorised into four different types based on their morphology, orientation and response to change in temperature (for schematic diagram see Fig. 4). All four LAB types discussed here were present before annealing began. Relevant information is summarised in Table 1. In the following section, these microstructures are described in detail.

3.2.1. Type 1 LABs

Type 1 LABs are long, continuous boundaries (average length for CDZ is 207 μm), while in the PZs the longest measured was over 1050 μm (and continued outside the analysis area). These boundaries are sub-parallel to one another and have misorientations
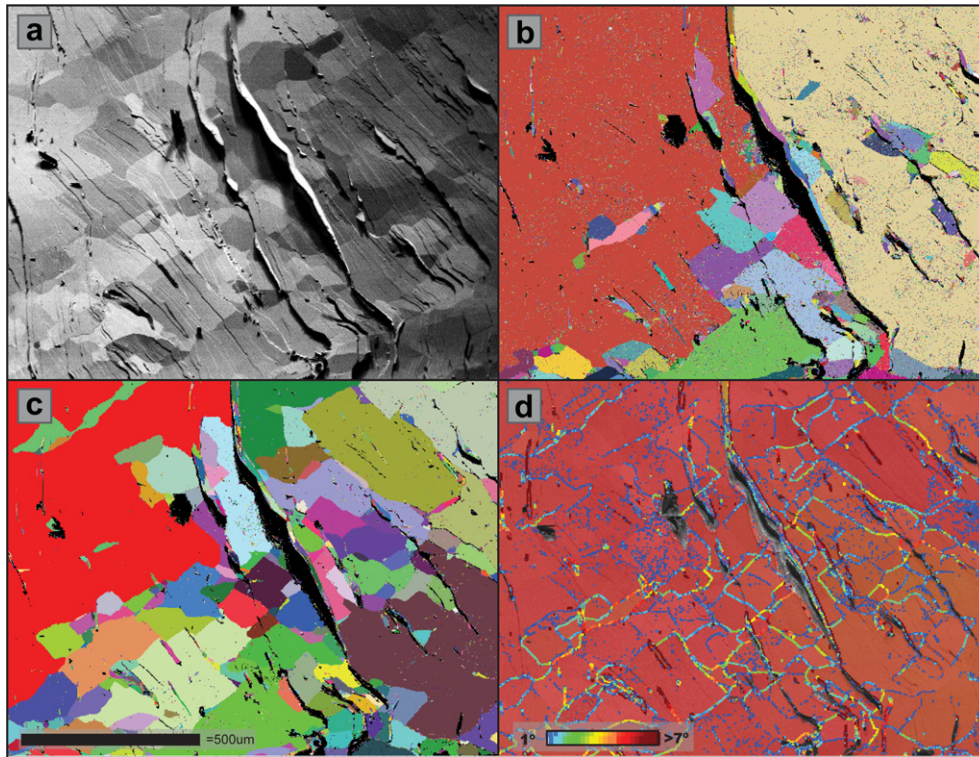
Fig. 3. Comparison of various noise reduction and filtering techniques with orientation contrast microstructure. (a) orientation contrast image. (b) EBSD data with grains in random colours after noise reduction. (c) EBSD data with grains in random colours after noise reduction and the application of two passes of the Kuwahara filter using pre-grain detection of 5° with boundary closure to 0, and a smoothing angle of 1.5°. (d) subgrain boundaries overlaying a band contrast image and inverse pole figure colouring. The misorientations of boundaries are represented by a continuous gradient of colours, given in the key.

larger than 3°. They also tend to be straighter for longer lengths than other LABs (Figs. 4 and 5j). These LABs are particularly well developed in the PZ, while in areas examined from the CDZ, they tend to form the sides of more equiaxed subgrains.

Misorientation axis analysis (Fig. 5a and j) indicate that type 1 rotation axes are parallel to [100]. Boundary trace analysis shows that boundary orientations are consistent with a tilt geometry because misorientation axes lie on the boundary trace, though we cannot entirely rule out the possibility of a twist geometry or a combination of tilt/twist (Lloyd et al., 1997; Prior et al., 2002). Type 1 LABs are aligned parallel to [011] or [0$\bar{1}$1] with (011)[0$\bar{1}$1] or (0$\bar{1}$1)[011] as possible slip systems (Fig. 5e). This fits with the slip systems theoretically activated during deformation (Fig. 1a).
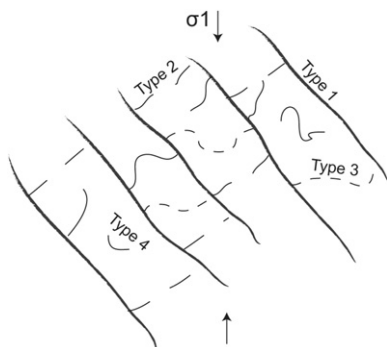
Fig. 4. Schematic of the four categories of LAB types.

3.2.2. Type 2 LABs

Type 2 LABs have a medium length (average 64 μm) and are also aligned parallel to [011] or [0$\bar{1}$1]. These boundaries are also very straight, often straighter than type 1, but not continuous for long distances as they are usually located between two type 1 LABs (Figs. 4 and 5j). They have medium to low misorientations (>1.5° and <3°).

The misorientation axes of type 2 LABs are also sub-parallel to [100] (Fig. 5b). Boundary trace analysis found that these LABs exhibited a similar geometry to type 1, with the misorientation axes lying on the boundary trace (Fig. 5f). Some combination of tilt/twist may exist, however a tilt geometry is most likely. Slip system analysis shows that type 2 LABs have the same possible slip systems as type 1 (Fig. 5f), although slip will always occur on the slip system perpendicular to that for type 1 LABs.

3.2.3. Type 3 LABs

Type 3 LABs generally lie sub-parallel to [010] and tend to be a mixture of very straight sections and slightly curved sections with a low to medium misorientation (>1.5° and <3°), and average length of 51 μm (Figs. 4 and 5k and l). These LABs were not observed in the PZ, and were found to be present only in the CDZ. Subgrains which are completely surrounded by type 3 LABs, or are bordered in some part by a type 3, have a higher aspect ratio, having an almost lensoid shape in appearance (Fig. 5l). This is in contrast to the typical equiaxed, diamond-shaped subgrains which are bordered by conjugate sets of type 1 and 2 boundaries and occur in the CDZ.

The misorientation axes of type 3 LABs are predominantly sub-parallel to [010], however, during annealing regime III their rotation axis changes to lie between [010] and [001] (presented in

Table 1
Summary table of the characteristics of the four different types of boundaries. Misorientation change rates stated are subject to an error of ±0.1.

LAB type	Type 1	Type 2	Type 3	Type 4
θmis (°)	>3	>1.5 < 3	>1.5 < 3	<2
Morphology shape/length	Straight/207–1050 μm	Straight/64 μm	Curved + straight/51 μm	Curved/8 μm
Alignment	‖ [011] or [0$\bar{1}$1]	‖ [011] or [0$\bar{1}$1]	sub - ‖ [010]	Random
Mis. axis	‖ [100]	‖ [100]	‖ [010]	No preferred
Behaviour				
Regime I	▲θmis ~0.4°/hr	▲ ▼θmis	▲θmis ~0.45°/hr	▲θmis
Regime II	▼θmis ~0.25°/hr	▼θmis ~0.31°/hr	▼θmis ~0.22°/hr	▼θmis
Regime III	▲θmis ~0.16°/hr	▲θmis ~0.39°/hr	▲θmis ~0.18°/hr Changed rot. axis	Dissipated

θmis - misorientation angle, ▼-decrease, ▲-increase, ▲▼or both.

Section 3.3). Boundary trace analysis shows that type 3 LABs slip along the second set of activated {110} slip planes, (101)[$\bar{1}$01] and ($\bar{1}$01)[101] (Fig. 5g and h). Trace analysis suggests that type 3 LABs are also tilt walls as the rotation axis lies on the boundary trace.

3.2.4. Type 4 LABs

Type 4 LABs have traces with random orientations and no preferred misorientation axis. They are generally more curved than other LAB types, occurring as shorter (average length of 8 μm) segments with a low misorientation angle (<2°) (Figs. 3d and 4). Type 4 LABs are primarily defined by their size and short length, of a few pixels. Boundary trace analysis was not possible for these LABs as they are curved and only occur as segments.

3.2.5. Moving boundaries

Members of types 1, 2 and 3 LABs have been observed to move during annealing (Fig. 6). The LAB sections which move are always part of a well-defined subgrain. Significant boundary movement was observed in two of the experiments (TL1_A2 and TL1_D1) with parts moving by up to 20 μm distance measured perpendicular to the boundary trace.

From boundary trace analysis it was found that these LABs were probably tilt boundaries as their rotation axis lay on the boundary trace (Fig. 6).

3.3. Annealing behaviour

The annealing behaviour of halite was divided into three distinct, temperature-dependent regimes. Individual regimes are characterised by specific LAB behaviour and changes in the substructure. In general, heating resulted in the reduction of crystallographic variation in the sample (Fig. 7). The highest rates of reduction of crystallographic variation occur between 280 and 300 °C. The effect of the small but significant changes in the LABs is summarised in relative boundary misorientation distributions (Fig. 8). This trend was observed in all samples that were subjected to all three heating regimes.

The different temperature-time paths investigated generally showed similar behaviour in all samples studied, with well-defined regimes occurring at the same approximate temperatures in each sample studied. However, in sample TL1_D2, which was heated directly to greater than 300 °C, regime I and II could not be distinguished and the behaviour recorded is that of regime III.

3.3.1. Annealing regime I

The first annealing regime (280–300 °C), results in an overall decrease in the crystallographic variation of the sample (Fig. 7). Characteristic behaviour during this regime can be divided into three main observations:

(a) LAB misorientations: LABs fall into two main categories dependent on change in misorientation. These are as follows:

(a1) Types 1 and 2 LABs (Fig. 9a and b): increase in misorientation. Type 1 LABs undergo a significant increase in misorientation (0.4°/h) (Table 1). Some type 2 LABs are also subject to a slight increase in misorientation (0.04°/h), while others undergo a decrease (0.17°/h), and (a2) Type 3 and 4 (Fig. 9c): decrease in misorientation. Type 3 LABs decrease by significant amounts (0.45°/h). Type 4 LABs almost universally decrease in misorientation with most dissipating completely. In summary, the decrease in misorientation of types 2, 3 and 4 outweighs the increase by type 1 and some type 2 LABs and the misorientation distribution shifts to a slightly higher ~5% relative frequency of LABs <1.3° (Fig. 8).

(b) LAB movement: Some LABs moved by as much as 7.7 μm with an average velocity of 5.1 μm/h.

(c) Rearrangement of internal subgrain structures: Parts of a subgrain rotate away from one another around a rotation axis between [001] and [010] (Fig. 10, shown for regime III). This eventually results in the formation of a new LAB and a subdivision of a single subgrain into several subgrains.

3.3.2. Annealing regime II

Regime II occurs at ~300 °C and is usually confined to one heating stage, although some of the characteristic behaviour can extend over a second stage. Behaviour is particularly characterised by the effect on the LABs, as now all types experience a decrease in misorientation (Fig. 9).

(a) LAB misorientations: Types 1, 2, 3 and 4 (Fig. 9): All LABs now experience a decrease in misorientation. Type 1 LABs decrease (0.25°/h), as well as Type 2 (0.31°/h) (Table 1). Type 3 LAB reduction continues, but at a reduced rate of decrease (0.22°/h). Type 4 LABs also continue to decrease, with many disappearing completely. This decrease is supported by the misorientation distribution in Fig. 8, where the percentage of LABs ~1.3° increases by approximately 20%, with a corresponding decrease in LABs >1.3°.

(b) LAB movement: LAB movement decreases significantly during this regime, with only minor migration observed, a maximum of 2.6 μm with a velocity of 1.92 μm/h.

(c) Rearrangement of internal subgrain structures: Internal subdivision of subgrains continues during this regime, including further development of new, very low angle subgrain boundaries with rotation axes between [001] and [010] (Fig. 10).

3.3.3. Annealing regime III

In regime III (>300 °C) all remaining LABs increase in misorientation (Fig. 9):
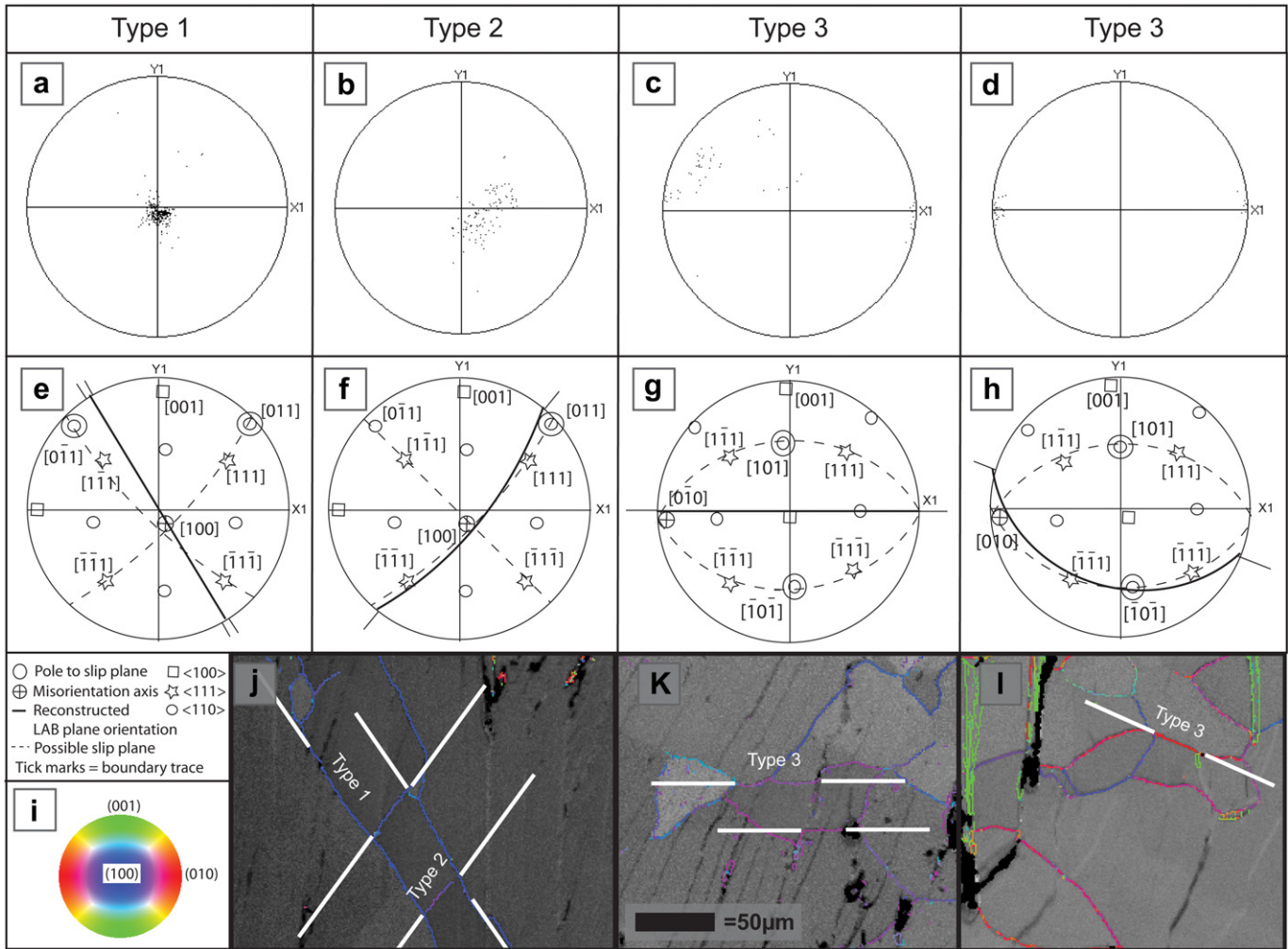
Fig. 5. Boundary analysis of types 1–3. (a)–(d) show equal area, lower hemisphere rotation axes scatters in sample co-ordinates pole figure plots for three of the LAB types. The compression axis is vertical for all images. It can be seen that type 1 and 2 have a rotation axes around [100] while type 3 are approximately around [010]. Rotation axes plots were also compared with small circle dispersions to make sure that the misorientation axes was determined accurately (not shown here). (e)–(h) show boundary trace analyses for the various LAB types. (e) the misorientation axis for a type 1 LAB lies on the boundary trace suggesting a tilt geometry. Slip system analysis suggests either (0$\bar{1}$1) [011] or (011) [01$\bar{1}$] (f) the misorientation axis for a type 2 LAB is similar to type 1. Slip system analysis indicates similar geometry to type 2, but slip will be along the opposite system. (g) The misorientation axis lies on the boundary trace suggesting a tilt geometry for type 3 LABs. Slip is along (101) [$\bar{1}$01] or the perpendicular ($\bar{1}$01) [101] (h) shows a second type 3 boundary analysis. This indicates a similar tilt geometry and slip system. (i) the pole figure legend for the misorientation axes images (j–l). (j–l) are maps showing the misorientation axes of LABs between 1 and 10° overlaying band contrast images. White lines indicate the boundary traces that have been selected for analysis in (e–h). (j) typical alignment and relationship between type 1 and 2 LABs. (k) type 3 LABs which are parallel to [010]. (l) type 3 LABs which are sub-parallel to [010].

(a) LAB misorientations: Type 1, 2 and 3 increase in misorientation (Fig. 9). The exception is type 4 LABs that have disappeared during the first two regimes. Type 1 LABs increase (0.16°/h), as well as Type 2 (0.39°/h) (Table 1). Most characteristic of this regime is the switching of type 3 LABs from decreasing to increasing in misorientation (0.18°/h). This is supported by the misorientation distribution (Fig. 8), which shifts to favour LABs >1.3° with a corresponding decrease in LABs ~1.3°. Type 3 rotation axes changes from predominantly [010], to a rotation closer to between [010] and [001] (Fig. 10).

(b) LAB movement: The LAB migration rate increases to ~10 μm/h with a maximum absolute movement of ~20 μm observed.

4. Discussion

4.1. Validity of results

It is important to note that though the changes in misorientation calculated during annealing are small and close to the

resolution limit, we believe they are significant. The results from ten experiments conducted on two crystals (five are reported here) showed similar regimes, lending statistical weight to the argument. A number of aspects of the experimental process may introduce errors into the results and it is thus important to discuss these here. During EBSD mapping, some damage to the surface of the sample from the beam occurs. In order to reduce this effect we used a fast indexing time (an average of 0.024s/pt). It is also fairly unlikely that the beam was applied to exactly the same spots so any beam damage would not have been compounded during the continuing heating stages. Heating to higher temperatures (~450 °C) caused extensive thermal grooving and redeposition on the sample surface. This was clearly seen in secondary electron mode of imaging (not shown here). For the temperature window in which these processes were investigated, the latter was not a problem, although in the slow heating experiment TL1_A1, some thermal grooving of boundaries did occur making it difficult to measure misorientations accurately.
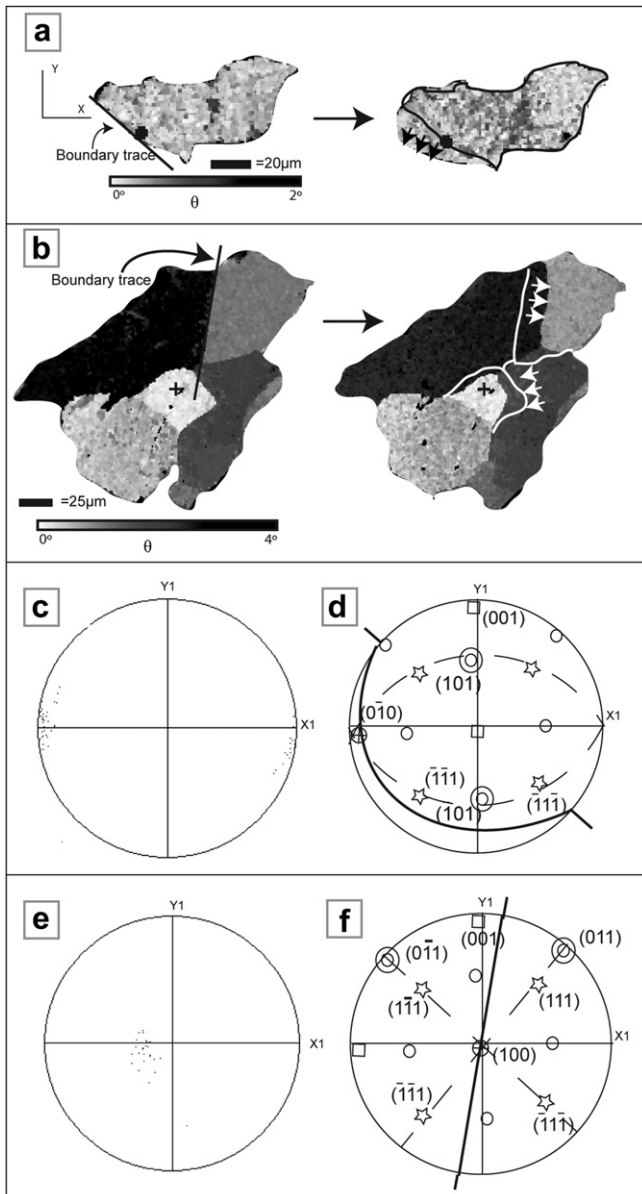
Fig. 6. Boundary trace analysis of moving LABs. The legend is the same as for Fig. 5. (a) and (b) are maps taken from TL1_A2 depict relative deviation in orientation with respect to a reference orientation (marked by cross). Movement of boundaries is shown by small arrows in the direction of movement and outlines of the original position of subgrain boundaries. Images on the left of the arrow are before heating and on the right are after heating ∼5 hr 20 min at 280–455 °C (c) and (e) are equal area, lower hemisphere stereonets showing the rotation axes for the boundaries selected in (a) and (b) respectively. Comparison with small circle dispersion taken around <100> and <110 > showed a similar misorientation axis as that used for boundary trace analysis (not shown here). (d) and (f) are equal area, lower hemisphere stereonets showing the boundary trace analyses for boundaries selected in (a) and (b) respectively. (d) shows that the boundary in (a) is a type 3 and has a tilt geometry with possible slip system (101) $[\bar{1}01]$ or $(\bar{1}01)$ $[101]$. (f) shows that the boundary in (b) is a type 1 or 2 with a probable tilt geometry and possible slip system $(0\bar{1}1)[011]$ or $(011)[01\bar{1}]$.

4.2. Substructural evolution during annealing

The results from the experiments on sample TL1 show that behaviour during annealing at lower temperatures in halite can be divided into three temperature-dependent regimes. Distinction between temperature regimes is based on the behaviour of different types of LABs during annealing, as well as the internal

rearrangement of the substructure within subgrains. LABs could be categorised into four different types based on annealing behaviour as well as distinctive morphological characteristics and orientation. It is suggested that annealing behaviour is highly dependent on both LAB type, and temperature of annealing. The results from the experimental data raise some interesting questions about the processes acting on the sample during annealing, especially since we cannot directly observe the dislocation behaviour. We present here a possible interpretation of these processes and how they interact. While we understand that this is not the only interpretation available and that parts of it are speculative, it is the authors' opinion that it is valuable to include it as a model to be tested in future work.

In the discussion on evolution during annealing reference is made to both annihilation occurring at the LAB sites and addition of dislocations into the LABs. For each regime, we suggest that one of these processes will dominate, which is reflected in the response of the LAB misorientation (i.e. increase or decrease). However, we see them as concurrently occurring processes in all LABs throughout annealing, with only the evidence of the dominant process observed. Our interpretation of the processes occurring throughout annealing within the various regimes is shown in Fig. 11.

4.2.1. Post-deformation substructure

It is evident from boundary analyses that LABs can be divided into two more general groups, those which are aligned with the primarily activated slip systems $(0\bar{1}1)[011]$ and $(011)[01\bar{1}]$ (type 1 and 2) and those which are formed by secondary slip along the slip systems $(101)[\bar{1}01]$ and $(\bar{1}01)[101]$ (type 3) (Fig. 5). Type 3 LABs are only present in the CDZ (Fig. 1c). They are not observed in the PZ (Fig. 1d) and this is likely to be due to bulging of the outer surface of the crystal allowing deformation to be accommodated. In the central regions, the additional stress can only be accommodated by the activation of the secondary slip systems, hence type 3 LABs are only found in this zone. Type 4 LABs were too curved and short to analyse successfully with boundary trace analysis (Lloyd et al., 1997; Prior et al., 2002).

From analysis of LABs as well as observations of behaviour during annealing regimes, a number of inferences can be made about the starting, post-deformation dislocation budget of the system. Slip system analysis indicates that there must be two main groups of dislocations present in the deformed sample, comprising primary slip dislocations (ρ_{ps}) from the initially activated slip systems, and secondary slip dislocations from the secondary slip systems (ρ_{ss}) (Fig. 1a). These slip systems are only activated together in the CDZ (Fig. 1c), not the PZ (Fig. 1d). Type 1 and 2 LABs are composed of ρ_{ps}, while type 3 LABs contain ρ_{ss}. Due to the probable tilt nature of the LABs it is likely that both ρ_{ps} and ρ_{ss} comprise predominantly edge dislocations. However, as some component of twist cannot be completely ruled out, it is probable that some fraction of the LABs are composed of screw dislocations. In regime I, the rate of decrease of type 3 LABs is similar to the rate of increase in type 1 LABs. Thus, though it is clear from the abundance of type 1 and 2 LABs that $\rho_{ss} < \rho_{ps}$ in the boundaries, the ratio of ρ_{ss} to ρ_{ps} is probably closer to 1 in the subgrain interior due to the similar rates of change.

4.2.2. Substructural evolution: regime I (280–300 °C)

We infer that, at the lower temperatures of regime I, dislocation movement is mainly by glide, with some possible cross-slip. In Type 1 LABs, dislocation addition into the boundary is the dominate process, resulting in an increase in misorientation. Concurrent annihilation is likely at the boundary sites, but is masked by the dislocation addition process. In type 2 LABs the two processes are
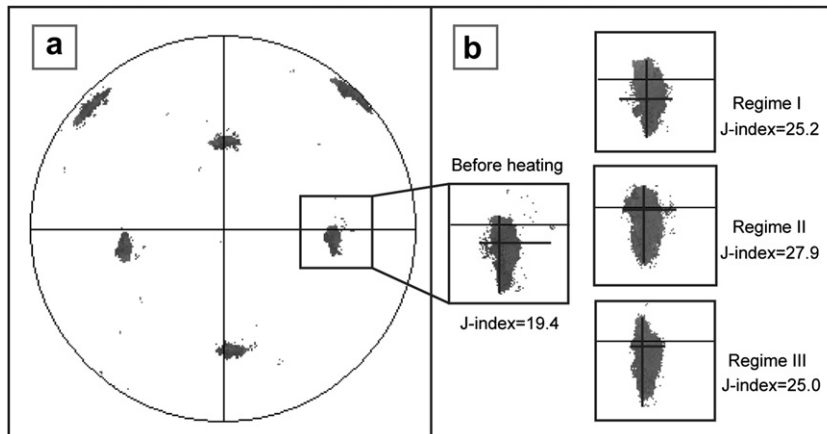
Fig. 7. Equal area, lower hemisphere pole figure taken during the annealing experiment on TL1_C1, indicating changes in crystallographic orientation variation. (a) shows the variation in crystallographic orientation before heating. (b) shows a zoomed in portion of the pole figure for each of the annealing regimes showing the decrease in crystallographic variation. *J*-index values are quoted showing the intensity of the texture. The *J*-index shows that during regime I and regime II the texture intensity increases, then decreases slightly in regime III. Black crosses show the size of the orientation spread and how it decreases throughout the annealing experiment.

on average fairly balanced, resulting in occasional small misorientation increase or decrease. Type 1 LABs are also more likely to attract dislocations due to their higher misorientation, and thus favourable low energy site (Hull and Bacon, 2001). Type 3 LABs experience a decrease in misorientation which is likely to be a result of annihilation at the boundary site. Type 4 LABs also decrease in misorientation (and in further annealing regimes dissipate entirely) which leads us to suggest that they are unstable, possibly made up of a less structured network of statistically trapped dislocations (Humphreys and Hatherly, 2004). Due to the large dislocation spacing they probably do not represent as attractive a site for dislocation addition as other LABs.

Two main processes are occurring in the subgrain interior: (a) Annihilation occurs as dislocations of opposite signs meet along the lattice planes. (b) In areas where dislocations of opposite sign are not available, dislocations of like sign begin to align into tilt walls, resulting the formation of new LABs.
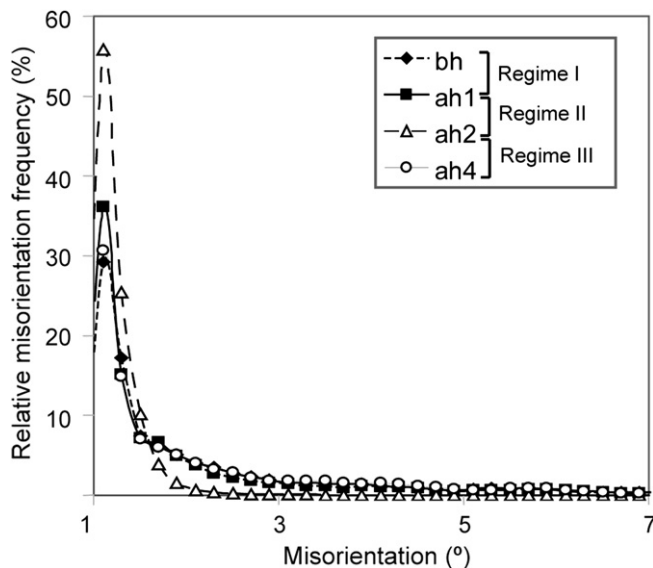
Fig. 8. The relative frequency (non-normalised) distribution of misorientation angles throughout the annealing experiment on sample TL1_C1. Distributions are calculated for the same area of the sample, an area of approximately 1769 by 925 pixels.

#### 4.2.3. Substructural evolution: regime II (∼ 300 °C)

When regime II is reached a significant change in behaviour occurs as type 1 and 2 LABs decrease in misorientation. An explanation for this invokes the behaviour of dislocations in a boundary setting. At lower temperatures, we infer that dislocation mobility is limited, with most movement occurring by glide and cross-slip. This process is limited by the higher activation energy of climb. Because dislocation climb is restricted, although dislocations can move into the boundaries, their separation cannot alter by dislocation climb within the boundaries to allow addition of more dislocations (Hull and Bacon, 2001). Hence, the boundary misorientation cannot continue to increase and we suggest some annihilation resulting in a misorientation decrease occurs. The rate of misorientation decrease in type 3 LABs is slower than in regime I (0.45°/h versus 0.22°/h). In our view, this change in rate is linked to the scarcity of ρ_{ss} present in the system due to annilihation in regime I. Type 4 LABs are absent due to their discussed dissipation during regime I.

4.2.4. Substructural evolution: regime III (>300 °C)

The difference in behaviour in regime III can be attributed to the fact that temperatures lie above the activation energy for climb (Franssen, 1993; Senseny et al., 1992). Accordingly, in type 1 and 2 LABs dislocations begin to rearrange within the boundaries, with spacing increasing by climb to accommodate new dislocation addition and misorientation increase. These processes are concurrent and will result in an overall decrease in dislocation spacing. In regime III, the rotation axis of type 3 LABs changes, as type 3 increases in misorientation. A possible explanation is that at higher annealing temperatures, most of the ρ_{ss} have been annihilated, ρ_{ps} could move into the type 3 LAB sites. It is suggested that in lower temperature regimes, while there may have been some addition of ρ_{ps} into these boundaries it is vastly outweighed by free ρ_{ss}. Once these have been mostly removed, the boundary site still represents an energetically preferable location. A possible explanation for the change in rotation axis is the addition of dislocations of both ρ_{ss} and ρ_{ps}. This is supported by the similar rotation axis of the new LABs formed in the subgrain interior, which we infer is likely to be a combination of ρ_{ss} and ρ_{ps}. By annealing regime III there are not enough free dislocations remaining in the system to initiate any new LAB formation.

4.2.5. Subgrain boundary movement

Movement of some subgrain boundaries was also observed. To move a boundary, it must be (a) mobile and (b) the movement must
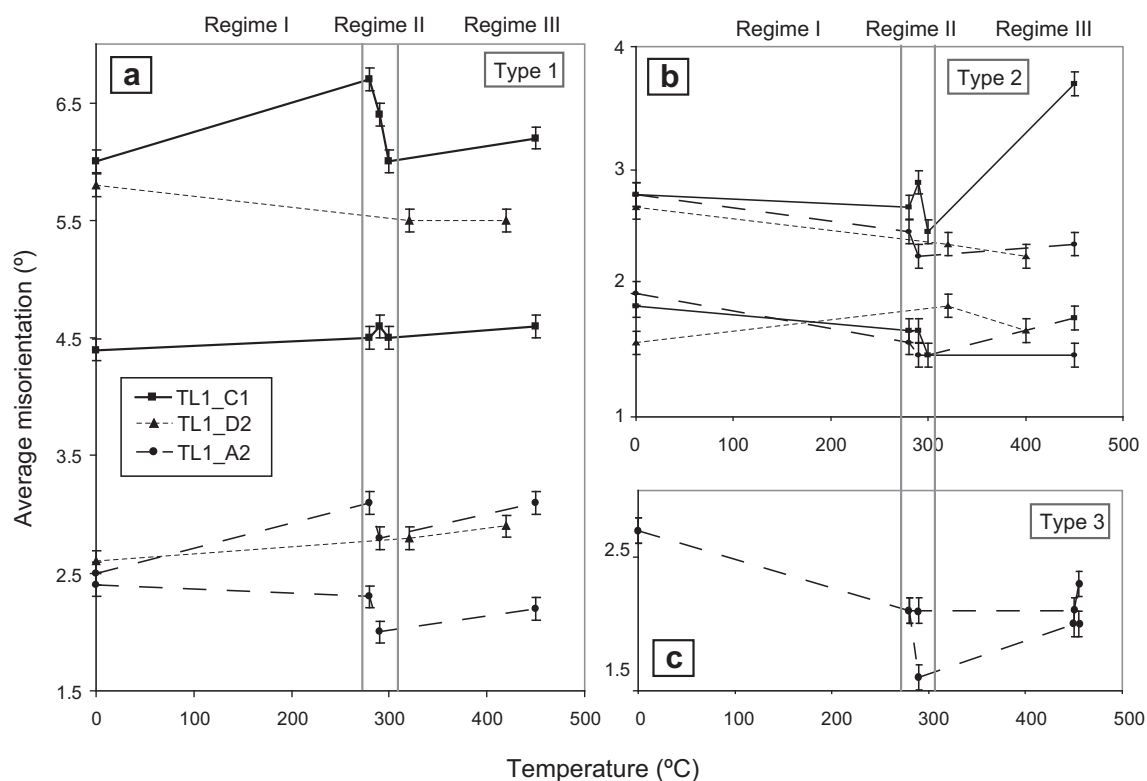
Fig. 9. shows the average of pixel-to-pixel misorientations directly adjacent to individual boundaries (see Fig. A1 for how this was calculated), before and after each heating stage in the three annealing regimes. While throughout the paper average misorientation rates are quoted, in Fig. 9 each line represents changes in a specific boundary. Error bars show the background error as well as the error associated with changes in indexing percentage (see App. 1 for further discussion). The values show small changes in the average misorientation angle for each of the heating regimes. (a) Type 1 LABs show an increase in regime I, followed by a decrease in regime II and increasing again in regime III. (b) Type 2 LABs show a misorientation increase in some boundaries and a decrease in others during regime I, a decrease in regime II and an increase in regime III. c) Only two Type 3 LABs are shown: both show a decrease in regime I, one LAB decreased further during regime II, the other did not change, both increased in regime III. The key in (a) applies to all boundaries.

result in energy reduction. Trace analysis shows that boundaries that moved are likely to be tilt boundaries, which indeed are known to exhibit a higher mobility than twist, or impure tilt/twist boundaries (Parker and Washburn, 1952). However, since most boundaries present are likely to have a tilt geometry further boundary mobility anisotropy may be present. If a boundary is mobile, the driving force is critical to its migration behaviour. The driving force is in the most general sense the energy reduction of the system, which in monomineralic materials is either reduction of the total boundary energy or stored energy i.e. dislocation density. In a crystalline material without stored energy differences and isotropic boundary energies, the driving force is directly related to boundary length. For instance, migration of both boundaries in Fig. 6b results in a decrease in total boundary length. If surface energies are anisotropic, however, the movement of a few specific boundaries may result in energy reduction; for example, the boundary in Fig. 6a is potentially moved to acquire an energetically favourable orientation: the lower energy orientation of a type 3 LABs (Piazolo et al., 2004). In our experiments, slight dislocation density differences which would drive grain boundary migration may be important; however, absolute or relative dislocation densities could not be determined.

4.3. Implications for interpretation of microstructures

This study has a number of important implications for the interpretation of microstructures affected by post-deformational annealing. In particular, these experiments as well as those completed by Bestmann et al. (2005) and Piazolo et al. (2006) have demonstrated that it is insufficient to view annealing in geological

materials as a classical progression. LABs cannot be grouped under one definition describing their behaviour during annealing, but must be divided based on the relationship between slip systems and the applied stress fields. Different types of LABs exhibited varying behaviour which was highly dependent on the character of the dislocations making up the boundary. During low temperature annealing (<300 °C), type 1 and some type 2 LABs showed a misorientation increase, while some type 2, type 3 and 4 LABs decreased or dissipated. We have shown that behaviour of the substructure can fluctuate before "normal" LAB development begins. With detailed analysis of the LABs, we can infer the post-deformational dislocation budget before and after annealing, which can potentially allow us to determine the annealing temperature.

An important aspect of this study is that it covers a range of temperatures that is not often investigated during annealing experiments, yet is a temperature window that is very relevant to geological settings. It must be stressed that although most behavioural changes in natural halite occur at lower temperature, the primary function for the choice of material in these experiments is as an analogue for other geological materials. The results indicate that annealing with a reduction in the overall crystallographic spread and a change in the subgrain structure by removal of dislocations can occur even if annealing takes place at temperatures below the deformation temperature. This is particularly interesting for natural settings where temperatures lower than that of deformation often prevail during exhumation of deformed rocks.

Results from this study can potentially allow us to recognise post-deformational annealing, using EBSD to infer the dislocation budget. At present, characteristics of the various regimes can only be recognised in this way if the deformation geometry is well-
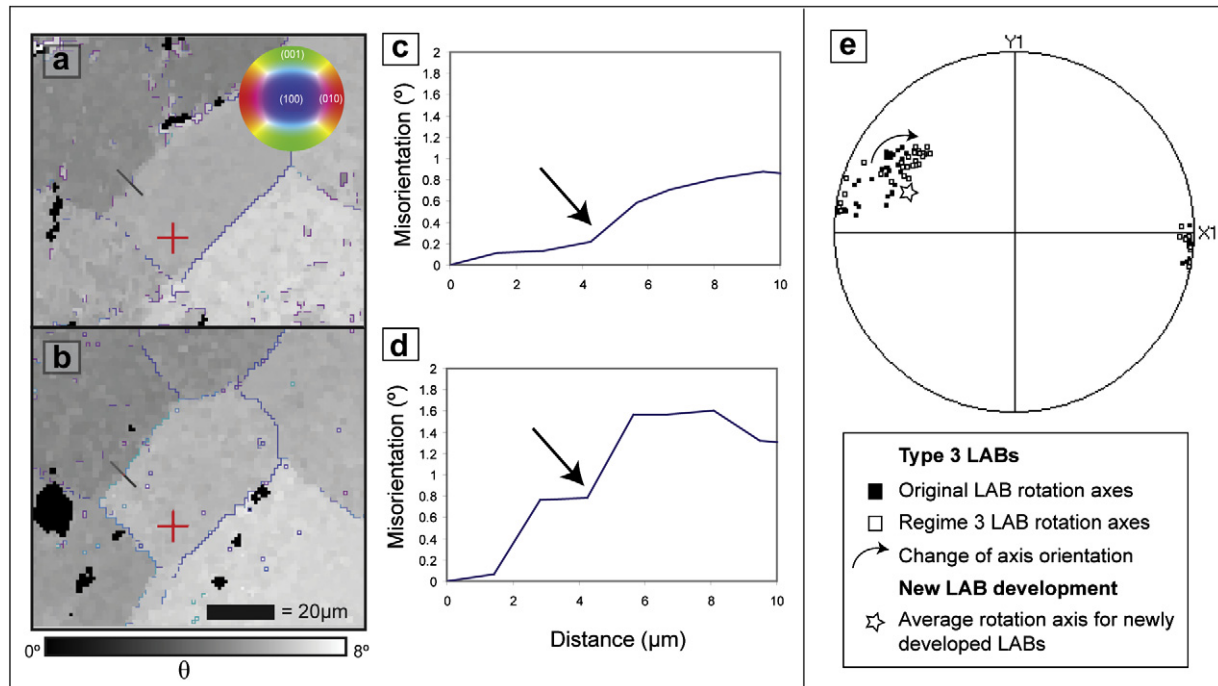
Fig. 10. Example of subgrain subdivision during annealing in TL1_A2. (a) and (b) maps depict relative deviation in orientation with respect to a reference orientation (marked by cross). Angular deviation for both maps is shown under (b). Maps are overlayed with boundary misorientation axis information. The pole figure legend is in box (a) and the scale bar for both images in box (b). The black line represents a misorientation transect, relative to the first point, which is shown in the graphs (c) and (d) corresponding to (a) and (b) respectively. Black arrows on the graphs point to evidence of subgrain subdivision. The maps were taken at different heating stages during the substructural development which are as follows: (a) before heating and (b) annealing regime III: after heating 5 hr 20 mins. (e) shows an equal area, lower hemisphere pole figure showing the original rotation axes of type 3 LABs overlayed by the new rotation axes from regime III. The arrow shows the general change in rotation axes of type 3 LABs. The rotation axes of new LABs created by subgrain subdivision is marked by a star for comparison.

known. We have discerned a number of features to look for when examining microstructures that may have undergone post-deformational annealing. We suggest that the noticeable changes to the substructure occur once climb has been activated, at temperatures above 300 °C. Important characteristics of post-deformational annealing above the climb activation temperature that will be apparent with EBSD include:

1) A lack of small boundary segments in the subgrain interior (type 4 LABs).
2) Rotation axes change in the less developed slip system LABs (in particular this requires an extensive knowledge of the deformation geometry and the preferred orientation of secondary LABs).

Other than this, the majority of changes result in an increase or decrease in the misorientation angle of the boundary and it is difficult to determine whether this has occurred when examining the final microstructure of a natural sample. We thus realise that there are limitations to this method when examining natural samples where the deformation geometry is not so well constrained.

We postulate that other materials should show similar behaviour at corresponding annealing temperatures. The major controlling factor of substructural behaviour during this stage of post-deformational annealing is the activation of dislocation climb, which occurs in halite at a homologous temperature above half the melting temperature (Tm = 1074 K) (Senseny et al., 1992). The results from our experiment correlated well with this reported activation temperature, with climb occurring at >0.53 Tm. Since this behaviour occurs within a well-defined temperature window with a traceable behaviour it should be possible to extrapolate the

results to other materials. Numerical simulation would be useful in testing our interpretation and attempting to apply results to other materials. Combination with other techniques, in particular the Weighted Burgers Vector calculation developed by Wheeler et al. (2009), with which it is possible to determine the dislocation density and the dominant burgers vector using EBSD data could assist with microstructural interpretation.

5. Conclusion

In-situ annealing experiments of pre-deformed salt single crystals at temperatures lower than that of deformation revealed three temperature-dependent regimes characterised by differences in low angle boundary behaviour and orientation changes in subgrains. According to behaviour during annealing, morphology and orientation different types of LABs could be distinguished with characteristics of most boundaries consistent with a tilt geometry. At low temperatures (280–300 °C) primary slip LABs increase in misorientation, while secondary slip LABs and LAB segments decrease. Average boundary velocities are 5 μm/h and subgrains begin to develop domains of like orientation. In contrast, at ~300 °C all LABs decrease in misorientation and boundary velocities are slower (2 μm/h), while subgrain division continues and results in new LAB formation. At temperatures above 300 °C, remaining LABs increase in misorientation and LAB velocity is markedly higher (10 μm/h).

Detailed boundary and EBSD data analyses allowed us to infer dislocation types in boundaries and subgrain interiors, as well as the starting dislocation budget of the system. We suggest that the temperature dependent behaviour during annealing can be directly linked to the distribution and availability of dislocations of different type and their mobility, related to the thermal activation of climb.
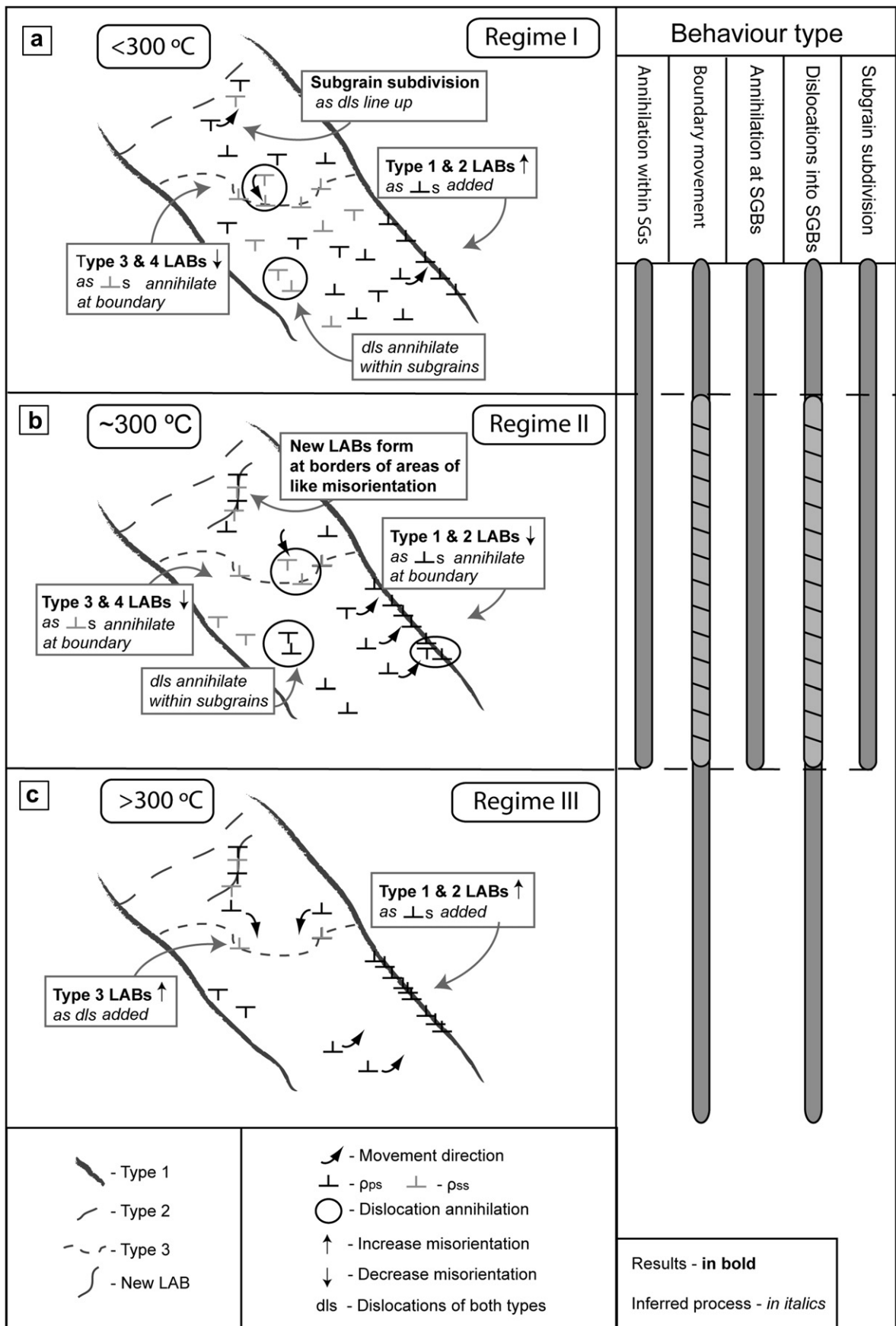
Fig. 11. Schematic depiction of the substructural evolution during annealing. To simplify we have demonstrated the behaviour on only type 1 (though type 2 are also shown) and 3 boundaries. (a) depicts processes occurring in annealing regime I, (b) annealing regime II, and (c) annealing regime III. The sidebar shows the different annealing processes and in which regimes they occur. The cross-hatched area indicates that inferred behaviour is weakened during that regime. For more details see text.

Processes responsible for changes are (a) annilihation of dislocations of opposite signs, (b) movement of free dislocations into existing and forming subgrain walls and (c) dislocation annihilation at LAB sites resulting in a misorientation decrease, as limited climb at lower temperatures influences the increase of dislocation separation within boundaries. Boundary movement is governed by anisotropies both in boundary energies and mobilities, resulting in only minor boundary movement, with migration rates strongly dependent on T.

These results are important for the future study of deformed rocks that have undergone annealing at elevated temperatures as it is shown that:

1) Annealing with reduction in crystallographic orientation and change in substructure occurs at temperatures below the deformation temperature
2) It is not enough to view annealing as a classical progression from dislocation annihilation to polygonisation with misorientation increase
3) Different LABs exhibit different annealing behaviour and must be investigated separately
4) Annealing behaviour is distinctly temperature dependent with correlation to activation of glide versus climb.

Acknowledgements

Appendix

Error calculation

In order to determine the background error we remapped three times over exactly the same area. The pixel-to-pixel misorientation average was then calculated for each map after the same noise reduction and filtering techniques were used as those applied in the experiments. The average was calculated (see Table A1) for both the whole area and a smaller area (138 by 133 pixels) which showed 100% indexing in all three maps. It is important to note that the whole area had non-indexed points even after noise reduction. For the whole area the variation in misorientation was found to be ±0.1 while for the small area it was ±0.001. The discrepancy in values may be largely based on the difference in indexing, so we believe that the error found for the whole area, of ±0.1 includes the inherent error from indexing at less than 100%. In our study we have thus reported the conservative error of ±0.1, though, as we have chosen mapped areas with a much higher indexing than 67% the error may be a lot lower than this in some cases. The method of boundary selection is also important as it may influence the average misorientation. We chose the LAB of interest using a precise method illustrated in Fig. A1. Subsets of subgrains on either side of the LAB of interest were chosen (Fig. A1a), which were then dilated by one pixel (Fig. A1b). The area covering both dilated subsets was then chosen, leaving an area of one pixel on either side of the boundary (Fig. A1c).

Table A1

Map number	Indexing (%)	Standard error	Average misorientation
Test 1 (whole area)	98.8	0.001	0.203
Test2 (whole area)	87.48	0.001	0.276
Test3 (whole area)	67	0.017	0.386
Test 1 (small area)	100	0.195	0.003
Test2 (small area)	100	0.198	0.002
Test3 (small area)	100	0.214	0.003
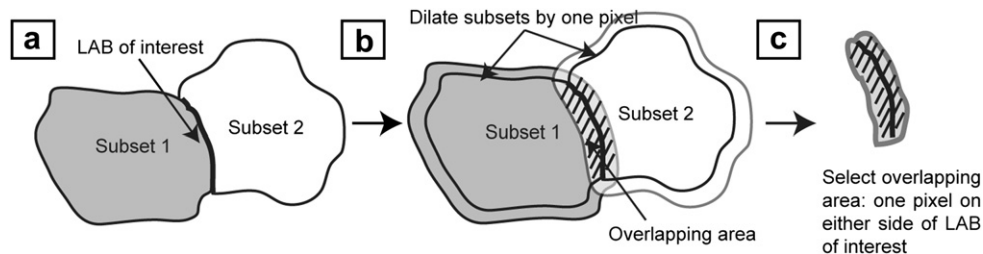
Fig. A1. The method of boundary selection of the areas used to calculate the average misorientation values in Fig. 9. (a) Two subsets are chosen either side of the LAB of interest. (b) subsets are dilated by one pixel. (c) the area where the subsets overlap is chosen as a new subset with one pixel either side of the LAB of interest. This area is used to calculate average misorientation values across the boundary.

Thermal expansion

The potential for thermal expansion affecting substructural behaviour due to the experimental setup was examined in a simple experiment. Due to the different expansion rates and amounts of halite and of the screwed-on brass plate holding the sample in place, there was the potential for addition of deformation in the sample due to bending. An undeformed, cleaved crystal of halite with a similar size as those used in the experiments was heated to temperatures of 300 °C and 450 °C. Once these temperatures were reached the sample was immediately cooled to 25 °C to preserve the structure. Long maps of ~16 pixels width (step size 2 μm) were taken, over approximately the same areas before heating and after the two heating stages, to investigate if significant bending occurred. Average pixel-to-pixel misorientation variation was calculated for ten areas of ~10 by 10. For the single crystal average misorientations values are, before heating: average $= 0.25°$

(standard error = 0.002), after heating at 300 °C: average = 0.26° (standard error = 0.002) and after heating at 450 °C: average = 0.29° (standard error = 0.001).

Misorientation transects (relative to the first point) were taken across the sample (Fig. A2). A cutoff of 1° was chosen in order to remove high angle data associated with non-indexed points and highlight any small, significant changes. From the results we see a slight increase in misorientation of 0.01° after heating to 300 °C and there were increases at some isolated points along the transect. The transect did not however, show significant bending of the crystal away from the clamp. At 450 °C, there was a general increase in the orientation spread, and an increase in the average pixel-to-pixel misorientation. This suggests thermal expansion may have occurred, but predominantly at higher temperatures (450 °C) and therefore it does not have a significant influence on this study.
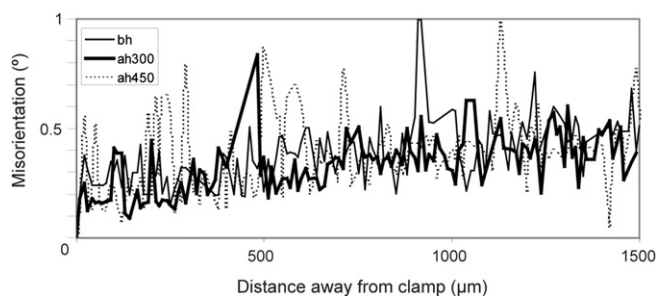
Fig. A2. Misorientation transects taken across the sample (relative to the first point). The sample is clamped by the brass screwed on plate at 0. The different lines represent transects taken across the whole sample before heating (bh), after heating at 300 °C (ah300) and after heating at 450 °C (ah450).

References

Baker, I., 2000. Recovery, recrystallization and grain growth in ordered alloys. Intermetallics 8, 1183–1196.

Barnhoorn, A., Bystricky, M., Burlini, L., Kunze, K., 2005. Post-deformational annealing of calcite rocks. Tectonophysics 403, 167–191.

Bestmann, M., Piazolo, S., Spiers, C.J., Prior, D.J., 2005. Microstructural evolution during initial stages of static recovery and recrystallization: new insights from in-situ heating experiments combined with electron backscatter diffraction analysis. Journal of Structural Geology 27, 447–457.

Bunge, H.J., 1981. Fabric analysis by orientation distribution functions. Tectonophysics 78, 1–21.

Davidge, R.W., Pratt, P.L., 1964. Plastic deformation and work-hardening in NaCl. Physica Status Solidi 6, 759–775.

Drury, M.R., Urai, J.L., 1990. Deformation-related recrystallization processes. Tectonophysics 172, 235–253.

Ferry, M., Humphreys, F.J., 1996. Discontinuous subgrain growth in deformed and annealed {110}<001> Aluminium single crystals. Acta Materialia 4, 1293–1308.

Ferry, M., Humphreys, F.J., 2006. Onset of abnormal subgrain growth in cold rolled {110}<001> oriented copper single crystals. Materials Science and Engineering A435–436, 447–452.

Field, D.P., Bradford, L.T., Nowell, M.M., Lillo, T.M., 2007. The role of annealing twins during recrystallization of Cu. Acta Materialia 55, 4233–4241.

Franssen, R., 1993. Rheology of synthetic rocksalt: with emphasis on the influence of deformation history and geometry on the flow behaviour. Geologica Ultraiectina 113.

Gottstein, G., 2004. Physical Foundations of Materials Science. Springer-Verlag, Berlin.

Guillope, M., Poirier, J.P., 1979. Dynamic recrystallization during creep of single-crystal halite: an experimental study. Journal of Geophysical Research 84, 5557–5567.

Heilbronner, R., Tullis, J., 2002. The effect of static annealing on microstructures and crystallographically preferred orientations of quartzites experimentally deformed in axial compression and shear. In: De Meer, S., Drury, M.R., De Bresser, J.H.P., Pennock, G.M. (Eds.), Deformation Mechanisms, Rheology and Tectonics: Current Status and Future Perspectives. Geological Society London Special Publications 200.

Huang, Y., Humphreys, F.J., Ferry, M., 2000. The annealing behaviour of deformed cube-oriented aluminium single crystals. Acta Materialia 48, 2543–2556.

Huang, Y., Humphreys, F.J., 1999. Measurements of grain boundary mobility during recrystallization of a single-phase aluminium alloy. Acta Materialia 47, 2259–2268.

Huang, Y., Humphreys, F.J., 2000. Subgrain growth and low angle boundary mobility in aluminium crystals of orientation {110}<001>. Acta Materialia 48, 2017–2030.

Huang, Y., Humphreys, F.J., 2001. Measurements of subgrain growth in a single-phase aluminium alloy by high-resolution EBSD. Materials Characterization 47, 235–240.

Hull, D., Bacon, D.J., 2001. Introduction to Dislocations, fourth ed. Elsevier Ltd, Oxford.

Humphreys, F.J., 2001. Characterisation of fine-scale microstructures by electron backscatter diffraction (EBSD). Scripta Materialia 51, 771–776.

Humphreys, F.J., Bate, P.S., Hurley, P.J., 2001. Orientation averaging of electron backscattered diffraction data. Journal of Microscopy 201, 50–58.

Humphreys, F.J., Hatherly, M., 2004. Recrystallization and Related Annealing Phenomena, third ed. Elsevier Ltd, Oxford.

Kirch, D.M., Jannot, E., Barrales-Mora, L.A., Molodov, D.A., Gottstein, G., 2008. Inclination dependence of grain boundary energy and its impact on the faceting and kinetics of tilt grain boundaries in aluminium. Acta Materialia 56, 4998–5011.

Kuwahara, M., Eiho, S., 1976. Processing of radioisotope angiocardiographic images. In: Preston, K., Onoe, M. (Eds.), Digital Processing of Biomedical Images. Plenum Press, New York, pp. 187–203.

Le Gall, R., Liao, G., Saindrenan, G., 1999. In-situ SEM studies of grain boundary migration during recrystallization of cold-rolled nickel. Scripta Materialia 41, 427–432.

Lens, A., Maurice, C., Driver, J.H., 2005. Grain boundary mobilities during recrystallization of Al-Mn alloys as measured by in situ annealing experiments. Materials Science and Engineering A 403, 144–153.

van der Linden, T.J.M., 2002. Deformation dependent conductivity of sodium chloride. Unpublished Msc. thesis. UtrechtUniversity.

Lloyd, G.E., Farmer, A.B., Mainprice, D., 1997. Misorientation analysis and the formation and orientation of subgrain and grain boundaries. Tectonophysics 279, 55–78.

Mainprice, D., Silver, P.G., 1993. Interpretation of SKS-waves using samples from the subcontinental lithosphere. Physics of the Earth and Planetary Interiors 78, 257–280.

Mirpuri, K., Wendrock, H., Wetzig, K., Szpunar, J., 2006. Behaviour of (111) grains during the thermal treatment of copper film studied in situ by electron backscatter diffraction. Microelectronic Engineering 83, 221–235.

Parker, E.R., Washburn, J., 1952. Transactions of the Metallurgical Society of AIME 194, 1076.

Passchier, C.W., Trouw, R.A., 2005. Microtectonics, second ed. Springer-Verlag, Berlin.

Pennock, G.M., Drury, M.R., Trimby, P.W., Spiers, C.J., 2002. Misorientation distributions in hot deformed NaCl using electron backscattered diffraction. Journal of Microscopy 205, 285–294.

Piazolo, S., Sursaeva, V.G., Prior, D.J., 2004. Grain growth in Al: first results from a combined study of bulk and in-situ experiments using a columnar structured Al foil. Materials Science Forum 467-470, 935–940.

Piazolo, S., Sursaeva, V.G., Prior, D.J., 2005. The influence of triple junction kinetics on the evolution of polycrystalline materials during normal grain growth: new evidence from in-situ experiments using columnar Al foil. Zeitschrift Fur Metallkunde 96, 1152–1157.

Piazolo, S., Bestmann, M., Prior, D.J., Spiers, C.J., 2006. Temperature dependent grain boundary migration in deformed-then-annealed material: observations from experimentally deformed synthetic rocksalt. Tectonophysics 427, 55–71.

Prior, D.J., Trimby, P.W., Weber, U.D., Dingley, D.J., 1996. Orientation contrast imaging of microstructures in rocks using forescatter detectors in the scanning electron microscope. Mineralogical Magazine 60, 859–869.

Prior, D.J., Boyle, A.P., Brenker, F., Cheadle, M.C., Day, A., Lopez, G., Peruzzo, L., Potts, G.J., Reddy, S., Spiess, R., Timms, N.E., Trimby, P., Wheeler, J., Zetterström, L., 1999. The application of electron backscatter diffraction and orientation contrast imaging in the SEM to textural problems in rocks. American Mineralogist 84, 1741–1759.

Prior, D.J., Wheeler, J., Peruzzo, L., Spiess, R., Storey, C., 2002. Some garnet microstructures: an illustration of the potential of orientation maps and misorientation analysis in microstructural studies. Journal of Structural Geology 24, 999–1011.

Rempe, N.T., 2007. Permanent underground repositories for radioactive waste. Progress in Nuclear Energy 49, 365–374.

Schléder, Z., Urai, J.L., 2007. Deformation and recrystallization mechanisms in mylonitic shear zones in naturally deformed extrusive Eocene-Oligocene rocksalt from Eyvanekey plateau and Garmsar hills (central Iran). Journal of Structural Geology 29, 241–255.

Senseny, P.E., Hansen, F.D., Russell, J.E., Carter, N.L., Handin, J.W., 1992. Mechanical behaviour of rock salt: phenomenology and Micromechanisms. International Journal of Rock Mechanics and Mining Sciences and Geomechanics 29, 363–378. Abstracts.

Seward, G.G.E., Prior, D.J., Wheeler, J., Celotto, S., Halliday, D.J.M., Paden, R.S., Tye, M.R., 2002. High-temperature electron backscatter diffraction and scanning electron microscopy imaging techniques: in-situ investigations of dynamic processes. Scanning 24, 232–240.

Seward, G.G.E., Celotto, S., Prior, D.J., Wheeler, J., Pond, R.C., 2004. In situ SEM-EBSD observations of the hcp to bcc phase transformation in commercially pure titanium. Acta Materialia 52, 821–832.

Smith, C.S., 1948. Grains, phases and interfaces: an interpretation of microstructure. Transactions of the Metallurgical Society of AIME 175, 15.

Urai, J.L., Means, W.D., Lister, G.S., 1986. Dynamic recrystallization of minerals. In: Hobbs, B.E., Heard, H.C. (Eds.), Mineral and Rock Deformation: Laboratory Studies (The Paterson Volume). Geophysical Monograph of American Geophysical Union, vol. 36, pp. 161–200.

Wheeler, J., Mariani, E., Piazolo, S., Prior, D.J., Trimby, P., Drury, M.R., 2009. The weighted burgers vector: a new quantity for constraining dislocation densities and types using electron backscatter diffraction on 2D sections through crystalline materials. Journal of Microscopy 233, 482–494.